IET Microwaves, Antennas & Propagation

Research Article

IET Journals
The Institution of Engineering and Technology

Modelling of ultra-wide stop-band frequency-selective surface to enhance the gain of a UWB antenna

ISSN 1751-8725
Received on 14th June 2018
Revised 22nd October 2018
Accepted on 26th October 2018
E-First on 18th January 2019
doi: 10.1049/iet-map.2018.5426
www.ietdl.org

Priyanka Das[1] ✉, *Kaushik Mandal*[2]

[1]*ECE, University of Engineering and Management, West Bengal, India*
[2]*Institute of Radio Physics and Electronics, University of Calcutta, West Bengal, India*
✉ *E-mail: priyankadas131986@gmail.com*

Abstract: Here, an ultra-wide stop-band single-layer frequency-selective surface (FSS) with high-incidence angle independence has been proposed to enhance the gain of an ultra-wideband (UWB) monopole antenna. The unit cell ($0.2\lambda \times 0.2\lambda$) of the proposed FSS consists of four asymmetric rectangular patches with circular slots embedded in it. This concept of four slotted patches is conceived to achieve ultra-wide stop-band characteristic over 4.7–14.9 GHz. An equivalent lumped circuit model for the FSS is proposed to provide insight into the working nature of the FSS. A UWB monopole antenna is also designed and integrated with the proposed FSS. Ultra-wide stop-band single-layer FSS converts the omnidirectional pattern of the monopole antenna into a unidirectional one and thereby registers a significant increase in its gain by 4.5 dBi. The design concept has been discussed and experimentally verified using simulated and measured results.

1 Introduction

In recent years, the study and investigation of broadband frequency-selective surface (FSS) is widely in practice. There has been a remarkable advancement in the wireless communication with the advent of ultra-wideband (UWB) technology. An FSS is a printed array of metallic patches or apertures on a dielectric substrate which behaves as a spatial filter having specific reflection or transmission characteristics for the electromagnetic (EM) waves impinging on it. Its performance depends on frequency, polarisation, and the angle of incidence of the incident EM wave. The utility of FSS lies in its various applications like antenna radomes, radar cross-section reduction applications, polarisers, EM shielders, and absorbers [1]. The most important step in the design process of a desired FSS is the proper choice of constituting elements for the array. The overall frequency response of the FSS structure is determined by the type and geometry of the element, the parameters of the substrate, the presence or absence of superstrates, and inter-element spacing. It is desirable that the FSS is angularly stable when illuminated by EM wave with a large angle of incidence. For decades, many researchers have conducted studies on various designs of band-stop FSSs for different applications. Multiple band-stop FSSs [2–5] have been proposed by different research groups. Triple-band FSS [2] designed for GSM frequency bands using synthetic resonator, tri-band FSS [3] based on convoluted design covering 3.28, 4.2, and 5.4 GHz, a multi-layer multi-stop-band FSS [4] consisting of dogbones shaped patches, and a single-layer FSS [5] for WiMAX, WLAN, and X-band filtering have been proposed. FSS with ultra-wide stop-band characteristics [6–8] are also investigated closely. FSS with Dürer's pentagon pre-fractals patch elements [6] shows 7–12 GHz band-stop characteristic. A three-layered FSS [7] using rectangular patches with two notches provides an ultra-wide band-stop response covering 4.05–14.12 GHz. An FSS with the garland-like design [8] printed on either side of the dielectric substrate exhibits band-stop response over 7.04–10.55 GHz. Structures of these wide band-stop FSSs are either complex or consist of multilayers. FSS-based corner reflector [9] to enhance the performance of a dual-band monopole antenna in the 3 and 5.5 GHz band, a conformal FSS [10] for radiation diversity of monopole dielectric resonator antenna at 5 GHz, and a high-gain wideband circularly polarised antenna by employing an FSS [11] as a reflector have been studied. A UWB antenna when integrated with an FSS reflector gives an enhanced and stabilised gain over a wide bandwidth. Gain enhancement of a UWB antenna by using multioctave dual-layer FSS [12] and a single-layer FSS [13] consisting of a square loop element and a circular ring element have been reported. A dual-layer FSS has been used for the gain augmentation of umbrella-shaped [14] and leaf-shaped [15] UWB antenna. A UWB antenna backed by UWB-FSS reflector [16] for polarisation diversity application is also reported. FSS with great incidence angle independence up to 75° has been designed at 7 GHz by using cross-spiral patch and four H-shaped fractal parts in [17]. The FSS [18] designed by incurving the arms of conventional cross-dipole shape inside for X-band applications provides stable angular performance for incidence angles up to 60°. The use of metamaterial-inspired superstrate is another useful technique for the gain enhancement of microstrip antenna. Using a three-layer metamaterial superstrate [19] gain has been enhanced by 70–80% over a 3% impedance bandwidth only. Another three-layer metamaterial superstrate [20] improves the gain by 4 dBi over 21.8% impedance bandwidth while a split ring resonator (SRR) type metamaterial superstrate [21] increases the gain by 86% over a narrow operating bandwidth of 680 MHz. From the above-mentioned survey on metamaterial-inspired design, it is evident that most of the works are intended towards the gain improvement of narrowband antenna, but there are very few works related to the gain augmentation of UWB antenna.

It has been observed that in order to achieve ultra-wide band-stop characteristics complicated fractal structures and 3D unit cells are used for constructing the FSS. It has the disadvantage of increased size and complexity of the antennas, thus requiring large space and increasing the possibility of error by complicating the fabrication procedure. The present work deals with the design of a novel single-layer FSS for achieving UWB stop-band characteristics as it aids in miniaturisation.

In this article, a hybrid structured asymmetrical FSS is used to yield an ultra-wide stop-band response (4.7–14.9 GHz) having a fractional bandwidth of >100%. The unit cell dimension (0.2λ) of the proposed FSS is much smaller than the operating wavelength. The single-layer FSS is optimised using the FEM-based Ansys HFSS EM simulator to enhance the gain of a UWB antenna and to extend its usability over the entire UWB frequency range (4.7–14.9 GHz). Significant improvement of 4.5 dBi in antenna gain has been achieved with this low-profile FSS without compromising the impedance bandwidth of the UWB antenna. The equivalent circuit

model (ECM) of the proposed FSS is constructed and justified using the circuit-system-EM-co-simulation software, Advanced Design System (ADS-2009).

2 FSS design and analysis

The unit cell geometry of the proposed FSS is illustrated in Fig. 1. The unit cell size is 14 mm × 14 mm which is only 0.2 times the maximum operating wavelength. The proposed FSS is an array of four rectangular patches of different dimensions with circular apertures of varied dimensions perforated on the conducting metallic patches. The patches are printed on a single side of the FR4 substrate with relative permittivity (ε_r) = 4.4, thickness (h) = 1.6 mm, and loss tangent (tanδ) = 0.02. This design proposal exploits the possibilities to achieve ultra-wide stop-band response using an array composed by the association of four patch elements in conjunction with four apertures per unit cell. When the EM wave impinges on the surface, each element resonates and scatters energy around its resonant frequency. A large bandwidth is obtained by exploiting the staggering between the multiple resonances.

2.1 Design steps

As the intention of the authors is to design a wide stop-band type FSS for the gain augmentation of a UWB antenna, instead of a single element unit cell, four different elements are incorporated into a single unit cell without compromising the overall dimension of the unit cell. This is a novel approach in comparison to the reported wide stop-band FSS unit cells. This approach is conceived owing to the fact that the individual structure should resonate at a particular frequency which is slightly different from each other and hence, there will be four closely spaced resonances that will be staggered to produce a wide stop-band. The stepwise design procedure is discussed as follows:

Step 1: Consider a patch type rectangular-shaped resonating element which will resonate in the desired band. In order to achieve a band-stop response, there must be an additive effect of a low-pass filter and a high-pass filter [22]. Hence, the low-pass filter and high-pass filter must coexist in the same structure. Therefore, a rectangular/square patch with an aperture at its centre is chosen where the rectangular/square patch exhibits low-pass behaviour and the aperture exhibits high-pass behaviour. The combined structure behaves as a band-stop filter with a desired resonating frequency.

Step 2: Replicate the structure and modify its dimensions slightly so that it can exhibit stop-band characteristics just nearby the previous element. Now, to achieve a wide stop-band place, this duplicated structure nearby the previous one.

Step 3: Repeat step 2 till the desired stop-band is achieved due to staggering between the closely spaced resonances.

Step 4: Finally, optimise the dimensions of the structures to prevent undesired notches and stop-band responses to get the best response.

In this manner, the design of the proposed FSS unit cell has been finalised.

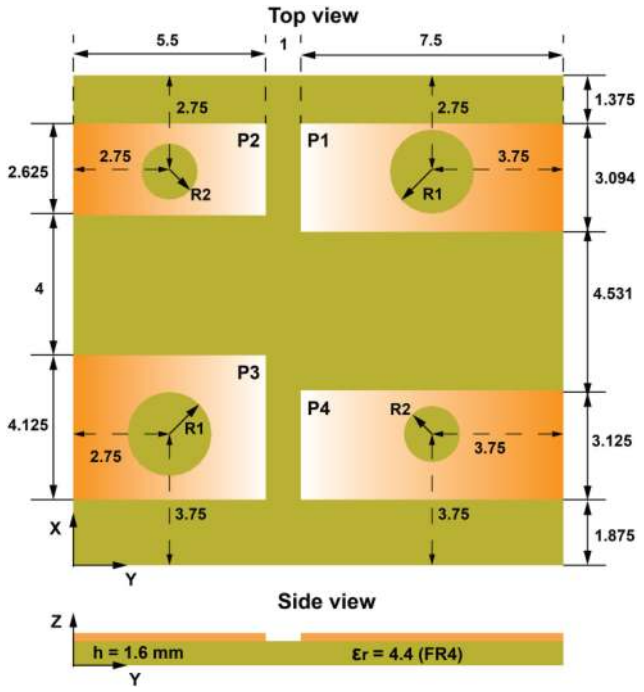

Fig. 1 *Unit cell geometry of the proposed FSS*

2.2 Evolution of the unit cell

A single patch with a circular aperture is considered as a one-patch (P1) unit cell. Then one by one, a two-patch (P1 + P2), a three-patch (P1 + P2 + P3), and finally, a four-patch (proposed) unit cell has been conceived depending on the transmission characteristics of Fig. 2*a*. The unit cell comprising one-patch only exhibits a narrow bandwidth. The two-patch unit cell shows a comparatively wider bandwidth. The three-patch unit cell yields a still wider stop-band, but it does not cover the entire UWB range. The UWB is obtained by exploiting multiple resonances of four patches. The transmission characteristics of the proposed unit cell with four patches cover the desired UWB (4.7–14.9 GHz). This analysis is made in HFSS using floquet ports with periodic (master/slave) boundary conditions which are used to simulate the infinite array. The periodic boundary conditions take into consideration, the coupling between the unit cells.

The FSS unit cell comprising more than four elements increases the size of the structure and makes it cumbersome unnecessarily. An ultra-wide bandwidth of 10 GHz is already achieved with four resonating structures. Hence, the requirement of more elements does not arise. Moreover, the simulation with five elements

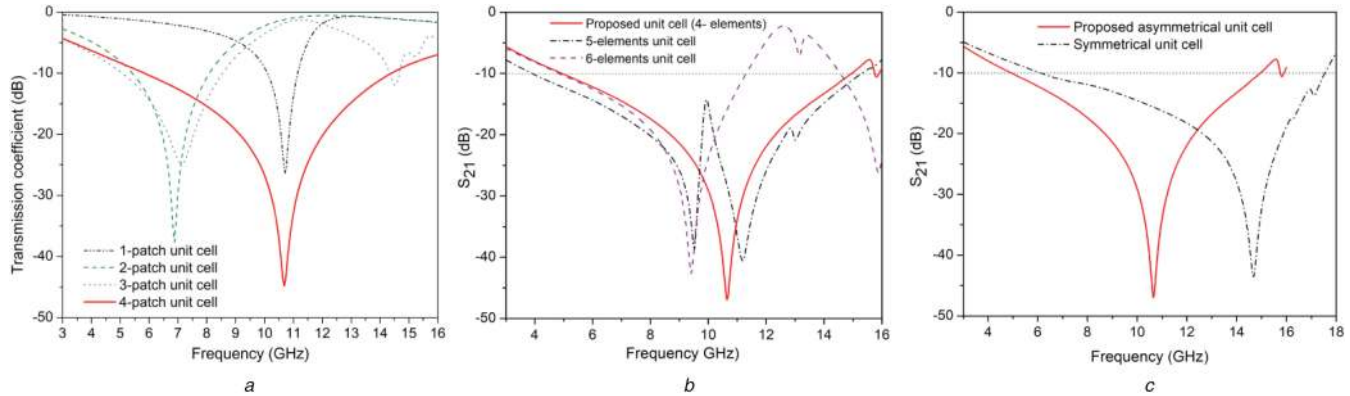

Fig. 2 *Transmission characteristics for the different configurations of unit cell*

(a) One-patch to four-patch unit cell, ***(b)*** Comparison between the proposed unit cell and five to six element unit cell, ***(c)*** Comparison between the proposed asymmetric unit cell and a similar symmetric unit cell

exhibits notch in the stop-band characteristic and the simulation with six elements decreases the bandwidth of operation, as shown in Fig. 2*b*. Hence, a four-element unit cell has been used for the FSS design.

The proposed unit cell of the FSS is not four-fold symmetric. During the design procedure, the same type of unit cell with symmetrical structure has been analysed and the corresponding response is presented in Fig. 2*c*. The band-stop response of the four-fold symmetric unit cell shows the resonance at 15 GHz which does not cover the desired ultra-wideband. Hence, the asymmetric structure has been retained as the FSS unit cell which covers the desired UWB.

Variation of the circular aperture's radius affects the stop-band performance significantly, as presented in Fig. 3. As $R1$ (radius of the larger circular aperture) and $R2$ (radius of the smaller circular aperture) are increased, the capacitive effect of the circular slots enhances due to its increased size; hence, the resonant frequency decreases because $f_r = 1/2\pi\sqrt{LC}$. A parametric study of the unit cell reveals that resonance occurs at 10.5 GHz with circular apertures of radius $R1 = 1.2$ mm and $R2 = 0.8$ mm. With the introduction of the slots, the current excited on the surface of unit cell is forced to flow surrounding the slots. In this way, the path length for current flow is increased, and the effective wavelength is also increased, leading to a reduced resonance compared to that for the patch without a slot.

The waves radiated by the antenna undergo change in the phase after getting reflected by the FSS. There is a linear variation of reflection phase of the FSS over the desired band with a steep rise near the resonant frequency 10.5 GHz. This is also illustrated in Fig. 3. The linear variation of the reflection phase of the proposed FSS accentuates the radiation of the UWB antenna when placed below it. If the reflection phase of the reflected waves decreases linearly with frequency then the waves radiated directly from the antenna, and the waves reflected by the FSS, are in-phase, which

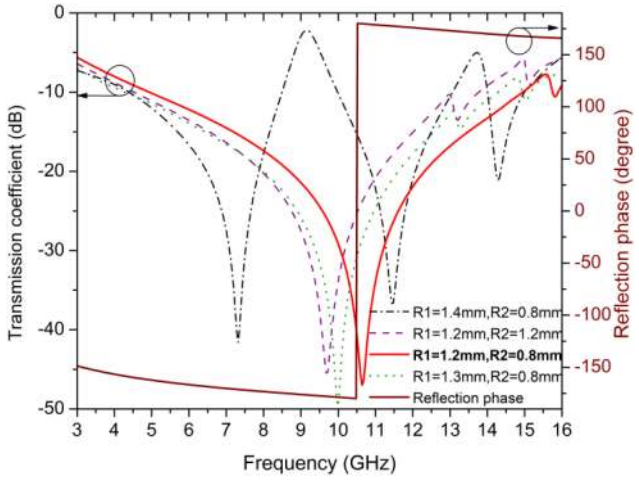

Fig. 3 *Transmission characteristic variation for different radius of circular slots and reflection phase variation with frequency*

leads to constructive interference. Accordingly, the resultant beams get collimated and the antenna gain is enhanced in the broadside direction. The consistency and linearity in the reflection phase response with linearly falling reflection phase helps to improve the radiation in the broadside direction which suggests antenna gain augmentation in the operational band.

2.3 Angular stability analysis

The angular stability performance of the proposed FSS is demonstrated at various incidence angles for both TE and TM polarisation in Fig. 4. The FSS structure exhibits nearly similar transmission characteristic at different incidence angles for both TE and TM polarisation. As the angle of incidence is increased from 0°, a slight lateral shift in the S_{21} response is obtained towards the left as becomes evident from the graph without significant change in the S_{21} response. The unit cell shows 0% shift in the resonant frequency at 20° angle of incidence, 3.42% shift in the resonant frequency for 40°angle of incidence, 7.22% shift in the resonant frequency for 60° angle of incidence, and 9.12% shift in the resonant frequency for 80° angle of incidence. The deviation of the resonant frequency is <10% for different incidence angles. Hence, the claim for angular stability 0°–60° has been made. The slight instability in the frequency response of the FSS for oblique incidence is caused by the asymmetry in the proposed design. The results reveal an almost stable response. However, for the incidence angles of >60°, slight changes in resonance frequencies around 10 GHz are observed that is due to the direct result of varying angular positions. As the overall stop-band is not influenced and remains almost stable and constant, these changes can be suitably neglected. Now, for the better understanding, both TE and TM polarisation characteristics are plotted in a single graph (Fig. 4*c*) for the incidence angle 0°–40° to avoid the clumsiness of the combined plot for all the incidence angles (0°–80°). For the variations of the angle of polarisation (ϕ) under normal incidence, the overall stop-band transmission response remains almost the same as shown in Fig. 5 and the resonant frequency shifted slightly for $\phi \geq 60°$ that may be due to the asymmetry of the unit cell.

2.4 Wave-port analysis

For wave-port analysis, an array of finite dimensions is considered. The periodicity of the printed pattern is kept much smaller than the wavelength of the operating frequency. To avoid grating lobes, the period is kept <0.5λ. The distance between the unit cells in the proposed design is kept as 3.25 mm which is ~0. 1λ. The period is defined to be the fixed inter-cell distance in the array [2] by the following equation

$$f_{go} = \frac{nc}{D(\sin\theta + 1)} \quad (1)$$

where θ is the incidence angle, c the speed of light, n the order of grating lobe frequency, and D the distance between the centres of two unit cells. The wave-port analysis is performed in HFSS with

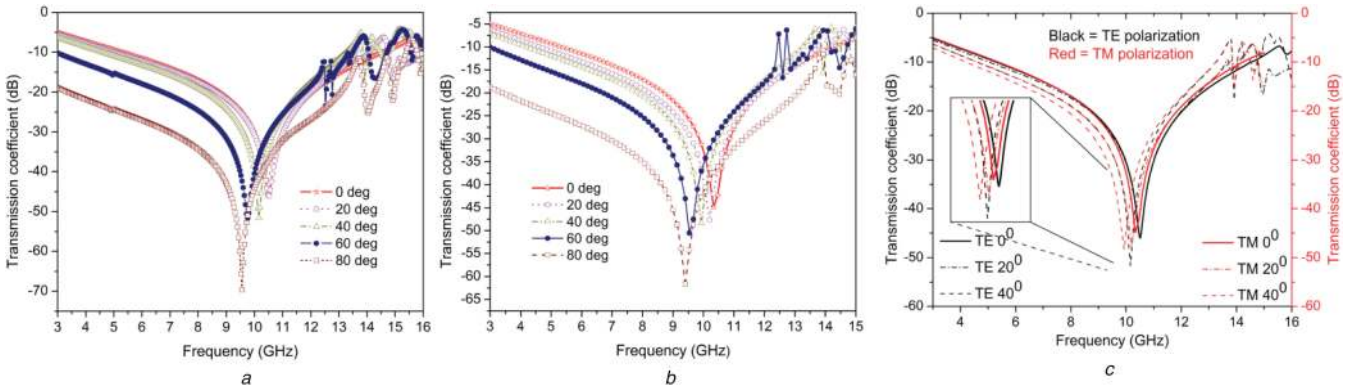

Fig. 4 *Variation of transmission characteristics for different incidence angles*
(a) TE polarisation, ***(b)*** TM polarisation, ***(c)*** Both TE and TM polarisation

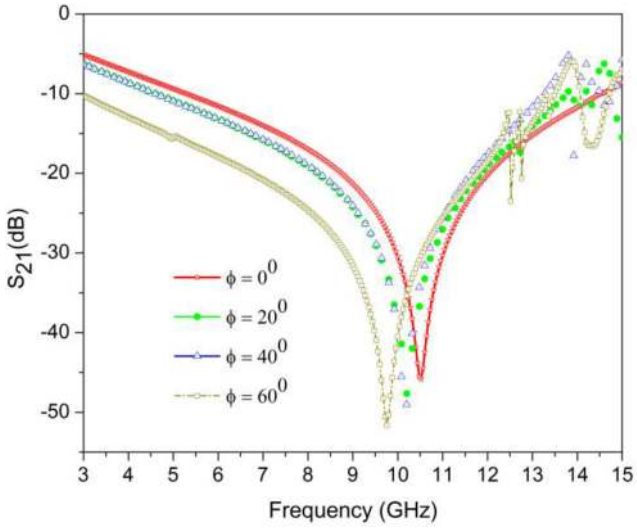

Fig. 5 *Variation of transmission characteristics for different polarisation angles under normal incidence*

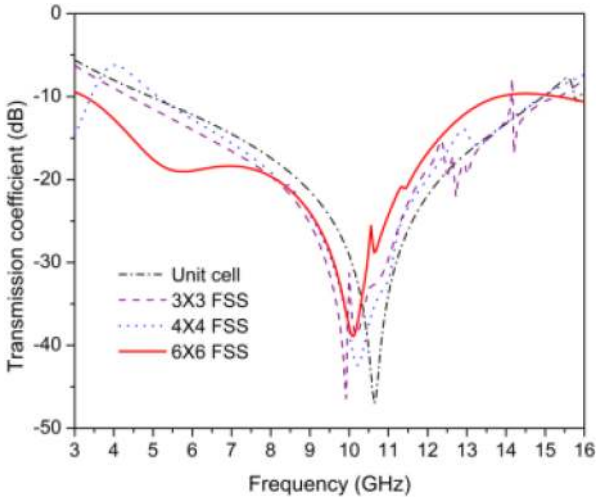

Fig. 6 *Variation of transmission characteristics for different size of FSS*

Table 1 Value of circuit components

L_1	C_1	L_2	C_2	L_3	C_3	L_4	C_4
0.20 nH	1.25 pF	0.25 nH	1 pF	0.05 nH	1.25 pF	0.17 nH	1.5 pF

different array size. It is found that with an increase in the dimension of the array, the S_{21} response of the FSS improves and approaches the response of floquet port analysis. For wave-port analysis, *E*-planes are placed opposite to each other and *H*-planes are placed opposite to each other. Transmission characteristics for different array size are summarised in Fig. 6. During the wave-port analysis, a 6×6 array has been analysed, but for the better measurement of FSS characteristics, an 8×8 array has been fabricated and integrated with the 20 mm × 27 mm UWB antenna. It is a fact that FSS dimensions should be of the order of aperture of the reference Horn antenna for better measurement results. That is why a large FSS (8×8) has been fabricated. At the time of integration of this FSS with the UWB antenna, one can consider the smaller array size which will not affect the enhanced antenna performances.

2.5 ECM of the FSS

The unit cell comprises four cells. Each cell consists of a rectangular patch having a circular aperture perforated in it. The unit cell acts as a hybrid resonating structure which behaves as a band-stop filter comprising an inductance and capacitance placed in series with each other. The circular apertures in the rectangular

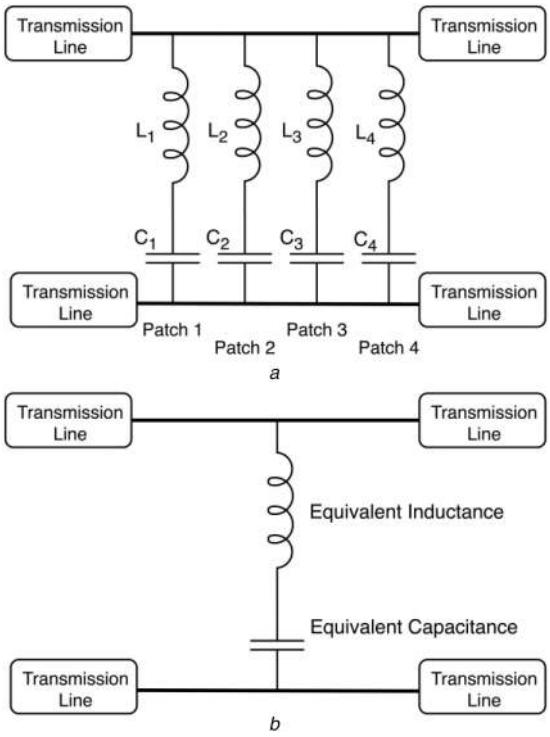

Fig. 7 *Circuit model of unit cell*
(a) Considering each element, ***(b)*** Equivalent model

patches have a capacitive effect in the overall response. The metallic patch portions in the unit cell have an inductive effect. On probing into the structure of the unit cell, it is found that there are four copper patches in unison with circular apertures of varied dimensions. Hence, they contribute as four inductances and capacitances, respectively, in the ECM. The capacitance of the FSS model is produced by the charges induced on the edges of adjacent patches by the incident plane wave. Moreover, the inductance of the model is produced by the current induced on the patches.

The dielectric substrate beneath the copper patches behaves as transmission line [23] sections on either side of the lumped circuit. The four resonators are connected in parallel to acquire a multiband performance. This equivalent circuit is shown in Fig. 7, which precisely models the frequency response of the FSS. This ECM of FSS is valid for normal and oblique incidences of a plane wave. The ECM comprises the lumped circuit cascaded with the transmission line sections on either side.

The proposed ECM is thoroughly analysed using ADS-2009. Different values of capacitance and inductance are assigned to obtain the transmission coefficient similar to that obtained in HFSS simulation. When there is a minimum difference between the responses (S_{21}) obtained from the HFSS and ADS circuit model, the best values of the elements are extracted. The optimised value of the circuit components is given in Table 1.

The inductance and capacitance of the microstrip line can be calculated using (2) and (3) as given in [24]

$$L = \mu \frac{P}{2\pi} \log\left(\frac{1}{\sin(\pi w/2P)}\right) \tag{2}$$

$$C = \varepsilon_0 \varepsilon_e \frac{2P}{\pi} \log\left(\frac{1}{\sin(\pi g/2P)}\right) \tag{3}$$

L is the strip inductance, which is determined by the strip length P, the strip width w, and the effective magnetic permeability μ of the structure. C is the capacitance between adjacent strips, which is determined by the strip length P, the gap width g between the strips, and the effective dielectric constant ε_e of the structure.

In the lumped circuit equivalent model, impedance of individual branch can be calculated using the following equations as given in [23, 25]

$$Z_i = \mathrm{j}X_i = \mathrm{j}\left(\omega_i L_i - \frac{1}{\omega_i C_i}\right) \tag{4}$$

where L_i and C_i are the inductance and capacitance of the ith branch.

$$\omega_i = \frac{1}{\sqrt{L_i C_i}}, \quad \text{and} \quad \omega_0 = \frac{1}{\sqrt{L_0 C_0}}$$

ω_0 is the resonant frequency of the equivalent LC circuit (Fig. 7*b*), L_0 the equivalent inductance, and C_0 the equivalent capacitance.

Transmission matrix of the FSS can be considered as

$$\boldsymbol{M}_{\mathrm{EC}} = \begin{bmatrix} 1 & 0 \\ Y_0 & 1 \end{bmatrix} \tag{5}$$

where $Y_0 = \mathrm{j}\omega C_0/(1-\omega^2 L_0 C_0)$, is the admittance of the equivalent lumped circuit.

$Y_i = \mathrm{j}\omega C_i/(1-\omega^2 L_i C_i)$, is the admittance of individual branch, $Y_0 = Y_1 + Y_3 + Y_4 + Y_5 = Z_1^{-1} + Z_3^{-1} + Z_4^{-1} + Z_5^{-1}$.

If l is the length of the transmission line section, then transmission matrix of the transmission line section [23] can be given by the below equation

$$\boldsymbol{M}_{\mathrm{TL}} = \begin{bmatrix} \cos\beta l & \mathrm{j}Z_L \sin\beta l \\ \mathrm{j}Y_L \sin\beta l & \cos\beta l \end{bmatrix} \tag{6}$$

where $Z_L = Z_0/\sqrt{\varepsilon_{\mathrm{r}}}$ is the characteristic impedance of the transmission line having a dielectric constant $\varepsilon_{\mathrm{r}} = 4.4$, and $Z_0 = 120\pi$ is the wave impedance in air.

The *ABCD* parameters of the transmission line sections in conjunction with the lumped circuit are found out by cascading the three sections and multiplying their *ABCD* matrices. Total transmission matrix can be obtained as

$$\boldsymbol{M}_{\mathrm{TOT}} = \begin{bmatrix} A & B \\ C & D \end{bmatrix} = \boldsymbol{M}_{\mathrm{TL}} \times \boldsymbol{M}_{\mathrm{EC}} \times \boldsymbol{M}_{\mathrm{TL}} \tag{7}$$

The transmission coefficients (S_{21}) of the FSS are obtained from the following equations

$$S_{21} = 2(AD - BC)/(A + B/Z_0 + CZ_0 + D) \tag{8}$$

As $(AD - BC) = 1$, for the reciprocal network, transmission coefficient (S_{21}) becomes

$$S_{21} = 2Z_0/(AZ_0 + B + CZ_0 + DZ_0) \tag{9}$$

$$\Gamma = \frac{A + (B/Z_0) - CZ_0 - D}{A + (B/Z_0) + CZ_0 + D} \tag{10}$$

where Γis the reflection coefficient and A, B, C, and D are the effective *ABCD* parameters of the complete circuit.

A MATLAB code is developed to compute the value of transmission coefficient using the aforementioned formulae in the frequency range 3–15 GHz. The result is compared with those obtained from ADS and HFSS in Fig. 8.

At the resonant frequency 10 GHz, the parameters from the equivalent lumped circuit using the above formulae are computed as follows:

$$\boldsymbol{M}_{\mathrm{TL}} = 1.0 \times 10^2 \times \begin{bmatrix} 0.0077 & 1.1432\mathrm{i} \\ 0 & 0.0077 \end{bmatrix}$$

$$Y = 0.0000 - 3.1216\mathrm{i}$$

$$\boldsymbol{M}_{\mathrm{EC}} = \begin{bmatrix} 0 & 0 \\ -3.1216\mathrm{i} & 1 \end{bmatrix}$$

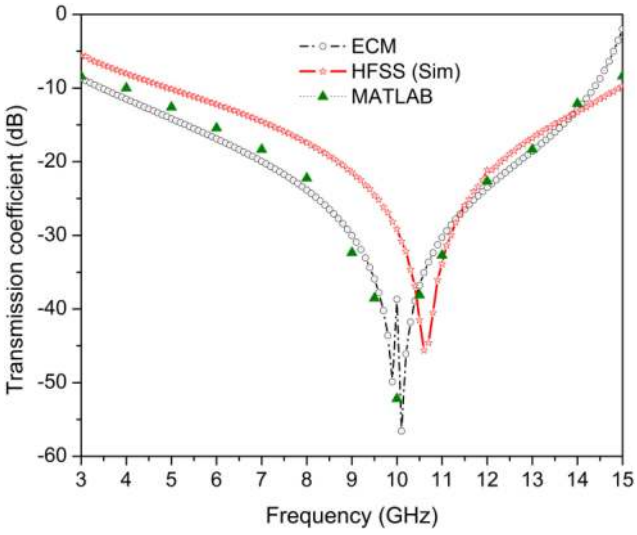

Fig. 8 *Comparison of transmission coefficient as obtained from ECM, HFSS, and MATLAB*

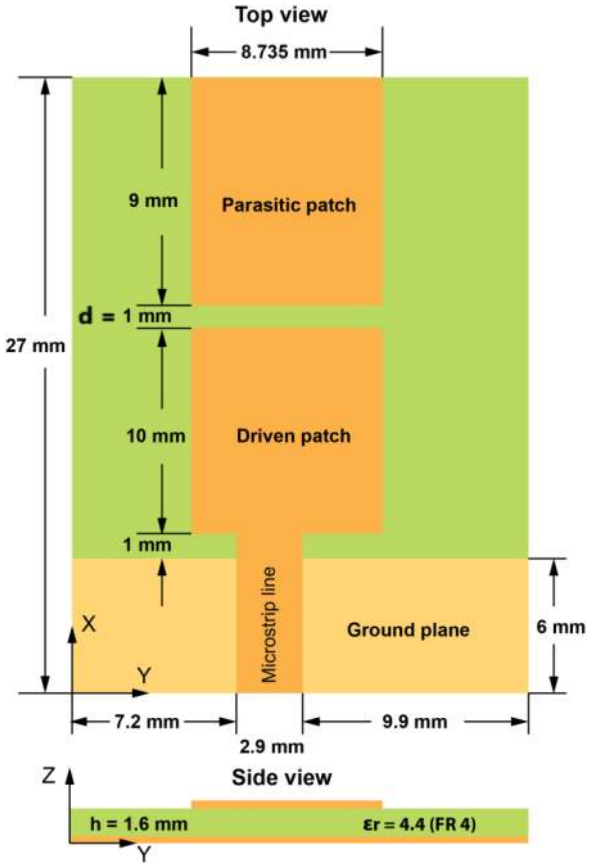

Fig. 9 *Structure of the UWB monopole antenna*

$$\boldsymbol{M}_{\mathrm{TOT}} = 1.0 \times 10^4 \times \begin{bmatrix} 0.0276 & 4.0969\mathrm{i} \\ -0.0002\mathrm{i} & 0.0276 \end{bmatrix}$$

$$S_{21} = -53.2\,\mathrm{dB}$$

This value is the same as that obtained from the S_{21} response from the ADS circuit using the optimised values of L_i and C_i, thus validating the proposed ECM.

3 Design and analysis of UWB antenna

The structure of the UWB monopole antenna is shown in Fig. 9. A parasitic patch is employed along with the main rectangular patch to improve the gain and impedance bandwidth of the monopole antenna. The antenna is fed using a microstrip line. As evident

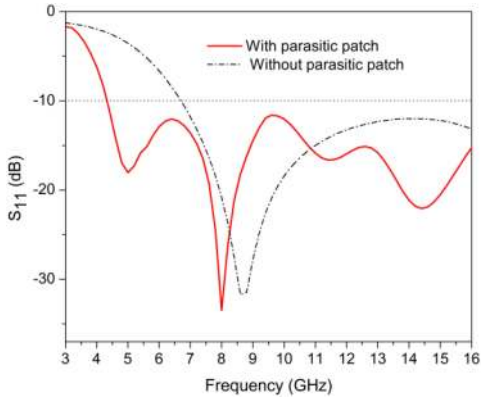

Fig. 10 *Effect of parasitic patch on the S_{11} characteristic*

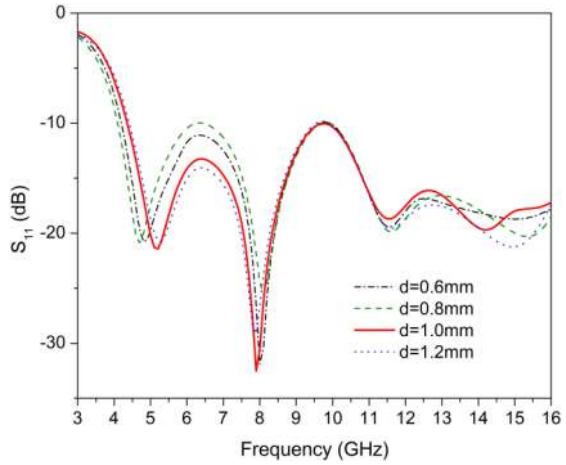

Fig. 11 *Gap (d) variation between the main and parasitic patch*

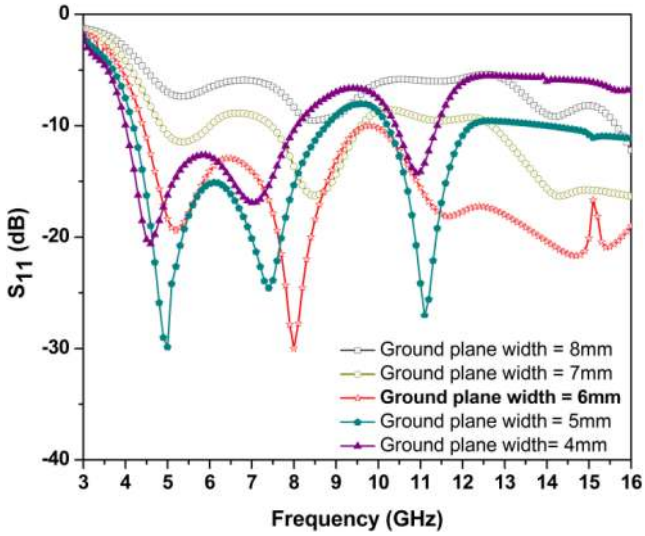

Fig. 12 *Effect of ground plane width variation on the S_{11} characteristic*

from the graph of Fig. 10, the antenna with the main patch only does not cover the lower frequencies of the UWB band, whereas due to coupling between main and parasitic patches, the proposed antenna covers 4–16 GHz with a resonant frequency at 8 GHz. The antenna length is approximately quarter wavelength at the resonant frequency. The inclusion of the parasitic patch enhances the operating bandwidth of the antenna. The main patch acting as a monopole antenna is cascaded with a parasitic patch which also acts as a monopole antenna.

The length of the main patch is optimised to 10 mm and the length of the parasitic patch is optimised to 9 mm with an optimal gap of $d = 1$ mm between them. As the gap between the main patch

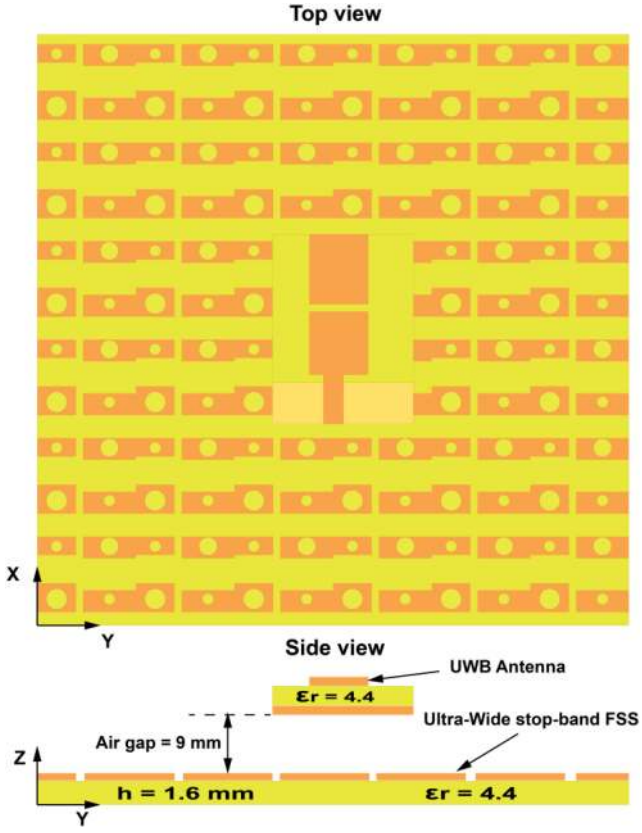

Fig. 13 *Illustration of FSS-integrated UWB monopole antenna*

and the parasitic patch is reduced, the S_{11} performance of the antenna deteriorates as shown in Fig. 11.

The distance between the radiating patch and the ground plane is an effective parameter for better matching of impedance since it affects the EM coupling between the lower edge of the patch and the ground plane. Depending on the results of Fig. 12, the width of the ground plane is optimised at 6 mm.

4 FSS-integrated UWB antenna

The proposed ultra-wide stop-band FSS is integrated with the proposed UWB monopole antenna, as shown in Fig. 13. To avoid coupling phenomena, the FSS must be placed at least $\lambda/2$ below the transmitting/receiving antenna. When the antenna is placed at a finite distance above the FSS, the wave radiated towards the FSS is reflected. This adds to the direct outgoing wave radiated from the antenna in the opposite direction to the FSS reflector. The gain of the antenna in the presence of the FSS reflector will be maximum when the two wave components add in phase giving rise to constructive interference. If φ_t is the phase of the wave transmitted from the antenna, φ_r is the phase of the wave reflected by the FSS, and φ_s is the roundtrip free space propagation phase delay between the antenna and FSS, then

$$\varphi_t = \varphi_r + \varphi_s \tag{11}$$

$$\varphi_s = 2 \times 2\pi f \times g/c \tag{12}$$

where g is the distance between the FSS and the antenna [12], and c the speed of light. For phase coherence, φ_t should be 0 or an integral multiple of 2π.

The distance between antenna and FSS layers is optimised for a higher flat gain response and better impedance matching over the entire frequency range of operation as presented in Fig. 14. In the parametric study, the distances are chosen close to 15 mm, which is $\lambda/2$ corresponding to the centre frequency (10 GHz) of the band. It is observed that the antenna with FSS achieves better impedance matching along with higher and stable peak gain for an air gap of 9 mm. The maximum peak gain of 9.4 dBi is achieved by

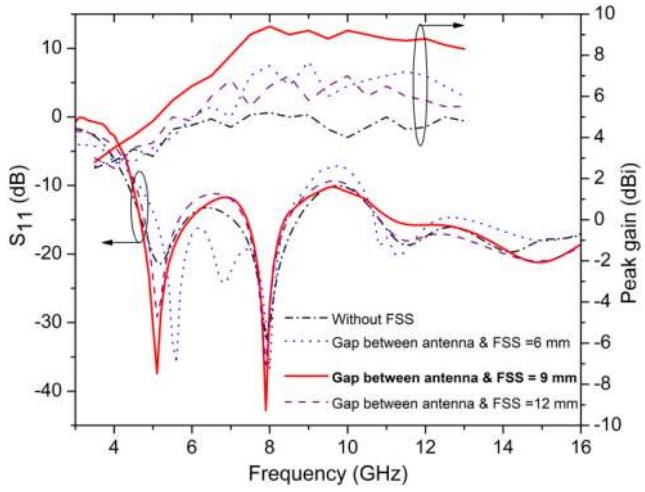

Fig. 14 *Change in S_{11} and peak gain due to gap variation between UWB antenna and FSS reflector*

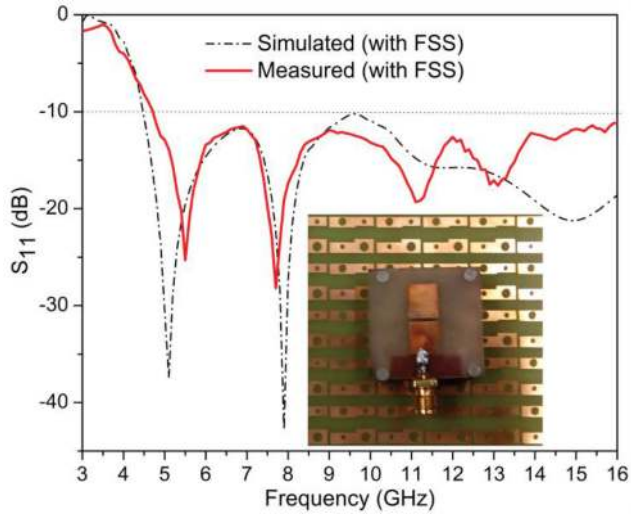

Fig. 15 *Simulated and measured S_{11} versus frequency characteristics (the fabricated design is shown in the inset)*

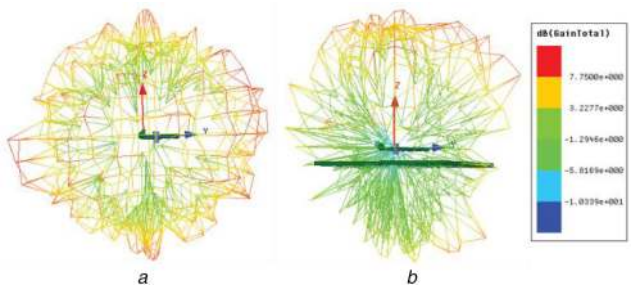

Fig. 16 *Three-dimensional plots of UWB antenna radiation*
(a) Without FSS, ***(b)*** With FSS

optimising the air gap between the antenna and FSS layer. The antenna coupled to FSS provides an impedance bandwidth of >100%.

5 Results and discussions

A prototype of the proposed FSS and UWB antenna are fabricated and integrated by maintaining an optimum air gap of 9 mm for the experimental verification purpose. The photo of this prototype is shown in the inset of Fig. 15. Simulated and measured S_{11} for the FSS-integrated UWB antenna is compared in Fig. 15, which shows good agreement. Minor variation can be seen between simulated and measured plots mainly due to cable loss and reflected waves from the surroundings.

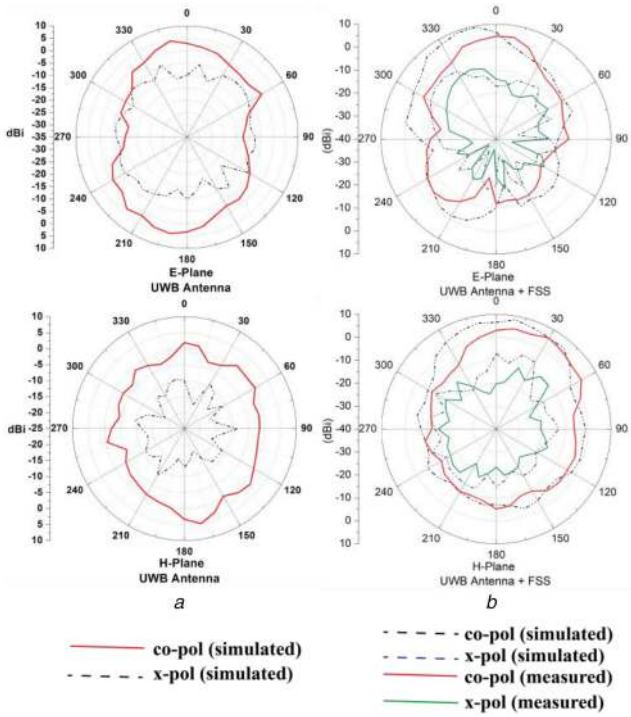

Fig. 17 *Radiation patterns of UWB antenna at 8 GHz*
(a) Without FSS, ***(b)*** With FSS

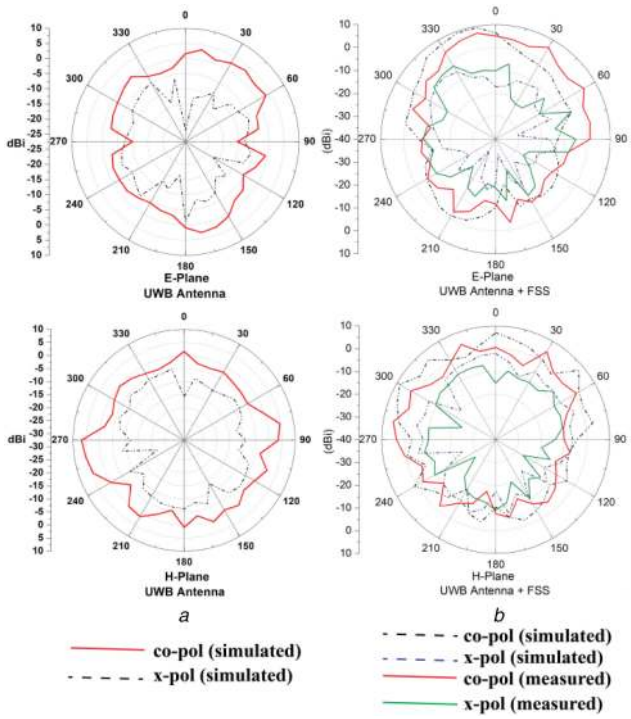

Fig. 18 *Radiation patterns of UWB antenna at 10 GHz*
(a) Without FSS, ***(b)*** With FSS

Three-dimensional polar plots of UWB antenna radiation with and without FSS are shown in Fig. 16, which confirm that the integration of FSS makes the UWB antenna directive.

Two-dimensional radiation patterns of UWB antenna at 8 and 10 GHz are shown in Figs. 17 and 18, respectively. These plots ensure that due to FSS, the radiation becomes directive. The gain of the UWB antenna increases significantly and become stable over the entire band as depicted in Fig. 19. Maximum improvement of the gain is 4.5 dBi when compared with the UWB antenna without FSS reflector.

The performance of the proposed FSS and FSS-integrated UWB antenna has been compared to the related articles and

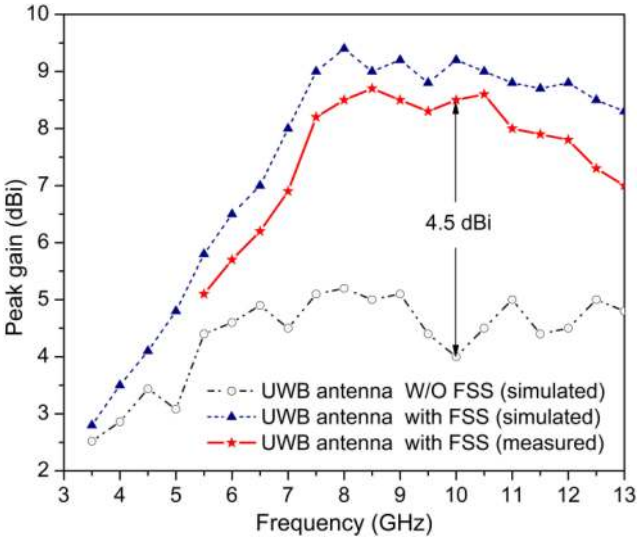

Fig. 19 *Peak gain versus frequency for different configurations*

Table 2 Performance comparison of the proposed design with some of the existing designs

Related works	Unit cell	Operating band, GHz	Gain of antenna without FSS, dBi	Gain of antenna with FSS, dBi	Incidence angle tolerances
[9]	0.165λ(single side)(11 × 11 × 1.2) mm^3	4.5–6.5	4.5	14.5	0–60°
[12]	0.17λ(multi-layer)(17 × 17 × 1.6) mm^3	3–12	6	10	—
[13]	0.09λ(single side)(8 × 8 × 0.635) mm^3	3.5–10.6	4	10.5	—
[14, 15]	0.1λ(dual layer)(10.6 × 10.6 × 0.8) mm^3 (upper layer) (10.8 × 10.8 × 0.8) mm^3 (lower layer)	3.05–13.4	4	8.5	—
[18]	0.2λ(multi-layer)(7.7 × 7.7 × 0.76) mm^3	8–12	—	—	0–60°
this work	0.2λ(single side, single layer)(14 × 14 × 1.6) mm^3	4.7–14.9	4.2	8.7	0–60°

summarised in Table 2. Since the dimensions of the FSS are compared in terms of their unit cell size rather than the array size, the unit cell dimensions of the related works have been mentioned. The dimension of the unit cell of the proposed FSS is only 0.2λ × 0.2λ corresponding to the lowest frequency (4.7 GHz) of operation, is much less than λ/4 which can be considered as reasonably compact. Now, referring to the comparison Table 2, the dimension of the proposed unit cell is of the same order or slightly higher than the other reported designs. It has been observed that in most of the previous FSS designs (except [13]), the authors have adopted the multi-layer approach to achieve wide stop-band. The unit cell of the proposed FSS comprises four different elements without compromising the overall dimension of the unit cell. This novel approach is conceived owing to the fact that the individual structure should resonate at a particular frequency which is slightly different from each other and hence, there will be four closely spaced resonances which will stagger to produce wide stop-band.

From the comparison table, it is evident that the gain augmentation performance of most of the works is nearly equal. Further, the most closely related works [12–15] did not show the angular stability performance of the FSS. However, the higher degree of incidence angle tolerance (angular stability) is essential for the FSS, and it is difficult to achieve over the wide band. The proposed FSS exhibits a higher order of angular stability over 0°–60°. The single-layer structure and higher angular stability are the main advantages of the proposed FSS in comparison to the previously published works.

6 Conclusion

Designs of a simple structured ultra-wide stop-band single-layer single-side FSS and a simple UWB antenna for UWB communication are described and analysed. An asymmetric type FSS unit cell is conceived for acquiring the wide stop-band performance. The proposed antenna with a single-layer FSS as a substrate exhibits a maximum of 107% increase in the peak gain over the more than 100% impedance bandwidth. The concept of parasitic patch along with main patch is adopted for UWB antenna design. The integration of this FSS as a back reflector to the UWB antenna converts the omnidirectional radiation pattern into a directive radiation pattern which results in a significant gain improvement of the UWB antenna. The analysis of ECM aids in better understanding of the working principle of the FSS. Stable incidence angle performance over the wide band is one of the key features of this design. Desirable radiation properties and a good agreement between simulations and measurements ensure the acceptance of this design for the UWB communication systems.

7 Acknowledgment

The authors would like to acknowledge Dr P.P. Sarkar, DETS, University of Kalyani, West Bengal, India, for providing measurement facilities.

8 References

[1] Munk, B.A.: '*Frequency selective surfaces: theory and design*' (Wiley, New York, 2000)

[2] Kartal, M., Golezani, J.J., Doken, B.: 'A triple band frequency selective surface design for GSM systems by utilizing a novel synthetic resonator', *IEEE Trans. Antennas Propag.*, 2017, **65**, pp. 2724–2727

[3] Liu, N., Sheng, X., Zhang, C., *et al.*: 'A miniaturized tri-band frequency selective surface based on convoluted design', *IEEE Antennas Wirel. Propag. Lett.*, 2017, **16**, pp. 2384–2387

[4] Xu, G., Hu, S.V., Eleftheriades, G.V.: 'A technique for designing multi-layer multi-stopband frequency selective surfaces', *IEEE Trans. Antennas Propag..*, 2018, **66**, pp. 780–789

[5] Bashiri, M., Ghobadi, C., Nourinia, J., *et al.*: 'WiMAX, WLAN, and X band filtering mechanism: simple-structured triple-band frequency selective surface', *IEEE Antennas Wirel. Propag. Lett.*, 2017, **16**, pp. 3245–3248

[6] Trindade, J.I.A., Silva, P.H.F., Campos, A.L.P.S., *et al.*: 'Analysis of stop-band frequency selective surfaces with Dürer's pentagon pre-fractals patch elements', *IEEE Trans Magnet.*, 2011, **47**, (5), pp. 1518–1521
[7] Segundo, F.C.G.S., Campos, A.L.P.S.: 'A design proposal for ultrawideband frequency selective surface', *J. Microw. Optoeletron. Electromag. Appl.*, 2013, **12**, pp. 398–409
[8] Baisakhiya, S., Sivasamy, R., Kanagasabai, M., *et al.*: 'Novel compact UWB frequency selective surface for angular and polarization independent operation', *Prog. Electromag. Res. Lett.*, 2013, **40**, pp. 71–79
[9] Chatterjee, A., Parui, S.K.: 'Performance enhancement of a dual-band monopole antenna by using a frequency selective surface-based corner reflector', *IEEE Trans. Antennas Propag.*, 2016, **64**, pp. 2165–2171
[10] Chatterjee, A., Parui, S.K.: 'Frequency-dependent directive radiation of monopole-dielectric resonator antenna using a conformal frequency selective surface', *IEEE Trans. Antennas Propag.*, 2017, **65**, pp. 2233–2239
[11] Kushwaha, N., Kumar, R.: 'Design of a wideband high gain antenna using FSS for circularly polarized applications', *Int. J. Electron. Commun. Eng.*, 2016, **70**, pp. 1156–1163
[12] Ranga, Y., Matekovits, L., Esselle, K.P., *et al.*: 'Multioctave frequency selective surface reflector for ultrawideband antennas', *IEEE Antennas Wirel. Propag. Lett.*, 2011, **10**, pp. 219–222
[13] Yahya, R., Nakamura, A., Itami, M.: 'Low profile UWB frequency selective surface based antenna', *ITE Trans. MTA*, 2016, **4**, (4), pp. 369–374
[14] Kundu, S., Chatterjee, A., Jana, S.K., *et al.*: 'A compact umbrella shaped UWB antenna with gain augmentation using frequency selective surface', *Electromagn. Radioeng.*, 2018, **27**, pp. 448–454
[15] Kundu, S., Chatterjee, A., Jana, S.K., *et al.*: 'Gain enhancement of a printed leaf shaped UWB antenna using dual FSS layers and experimental study for ground coupling GPR applications', *Microw. Opt. Technol. Lett.*, 2018, **60**, pp. 1417–1423
[16] Yahya, R., Nakamura, A., Itami, M.: 'A novel UWB FSS-based polarization diversity antenna', *IEEE Antennas Wirel. Propag. Lett.*, 2017, **16**, pp. 2525–2528
[17] Zhao, Z., Shi, H., Guo, J., *et al.*: 'A stop band frequency selective surface with ultralarge angle of incidence', *IEEE Antennas Wirel. Propag. Lett.*, 2017, **16**, pp. 553–556
[18] Kocakaya, A., Çakır, G.: 'Novel angular-independent higher order band-stop frequency selective surface for X band', *IET Microw. Antennas Propag.*, 2017, **12**, pp. 15–22
[19] Li, D., Szabó, Z., Qing, X., *et al.*: 'A high gain antenna with an optimized metamaterial inspired superstrate', *IEEE Trans. Antennas Propag.*, 2012, **60**, pp. 6018–6023
[20] Lin, J., Li, D.: 'A high-gain antenna with U-slot using zero-index metamaterial superstrate'. Int. Workshop on Antenna Technology: Small Antennas, Innovative Structures, and Applications (iWAT), 2017
[21] Arora, C., Pattnaik, S.S., Baral, R.N.: 'SRR superstrate for gain and bandwidth enhancement of microstrip patch antenna array', *Prog. Electromagn. Res. B*, 2017, **76**, pp. 73–85
[22] Sedra, A.S., Smith, K.C.: '*Microelectronic circuits: theory and applications*' (Oxford University Press, Oxford, UK, 2013, 6th edn., Chapter XI)
[23] Joozdani, M.Z., Amirhosseini, M.K.: 'Equivalent circuit model for the frequency selective surface embedded in a layer with constant conductivity', *IEEE Trans. Antennas Propag.*, 2017, **65**, pp. 705–712
[24] Sarabandi, K., Behdad, N.: 'A frequency selective surface with miniaturized elements', *IEEE Trans. Antennas Propag.*, 2017, **55**, pp. 1239–1245
[25] Liu, N., Sheng, X., Zhang, C., *et al.*: 'A design method for synthesizing wide band-stop FSS via its equivalent circuit model', *IEEE Antennas Wirel. Propag. Lett.*, 2017, **16**, pp. 2721–2725